




A Relationship between Stellar Age and Spot Coverage

Brett M. Morris 

Center for Space and Habitability, University of Bern, Gesellschaftsstrasse 6, CH-3012 Bern, Switzerland; morrisbrettm@gmail.com

Received 2020 January 31; revised 2020 February 20; accepted 2020 February 20; published 2020 April 16

Abstract

We investigate starspot distributions consistent with space-based photometry of F, G, and K stars in six stellar associations ranging in age from 10 Myr to 4 Gyr. We show that a simple light-curve statistic called the “smoothed amplitude” is proportional to stellar age as $t^{-1/2}$, following a Skumanich-like spin-down relation. We marginalize over the unknown stellar inclinations by forward modeling the ensemble of light curves for direct comparison with the *Kepler*, *K2*, and *TESS* photometry. We sample the posterior distributions for spot coverage with approximate Bayesian computation. We find typical spot coverages in the range 1%–10%, which decrease with increasing stellar age. The spot coverage is proportional to t^n where $n = -0.37 \pm 0.16$, also statistically consistent with a Skumanich-like $t^{-1/2}$ decay of starspot coverage with age. We apply two techniques to estimate the spot coverage of young exoplanet-hosting stars likely to be targeted for transmission spectroscopy with the *James Webb Space Telescope*, and estimate the bias in exoplanet radius measurements due to varying starspot coverage.

Unified Astronomy Thesaurus concepts: [Stellar photospheres \(1237\)](#); [Starspots \(1572\)](#); [Stellar rotation \(1629\)](#); [Bayesian statistics \(1900\)](#)

Supporting material: machine-readable table

1. Introduction

Stars are born rapidly rotating, and dappled with dark starspots in their photospheres (Berdugina 2005). Starspots are regions of intense magnetic fields that dominate over local convective motions to produce dim, cool regions in stellar photospheres. Starspot coverage shrinks from stellar youth into middle age. Young solar analogues like EK Dra (50 Myr) have hemispheric starspot filling factors in the tens of percent (Strassmeier & Rice 1998; Järvinen et al. 2018), while the Sun’s hemispheric spot coverage is roughly 0.03% at 4.6 Gyr (Morris et al. 2017). Many insights into starspots have been learned by analogy from observations of the Sun and its spots (Solanki 2003).

Stellar magnetic activity is perhaps most easily studied via stellar chromospheres, where magnetic active regions shine brighter than the mean photosphere, giving rise to strong emission lines like Ca II H and K, which correlate with magnetic activity. One of the pivotal observations of stellar magnetic activity was made by Skumanich (1972), using chromospheric emission line observations from O.C. Wilson. Skumanich showed that Ca II H and K intensities decay as $t^{-1/2}$, and provided observational evidence that stellar rotation is a key feature that drives stellar magnetic dynamos. Many patient observers have carried on studies of stellar chromospheric activity over the last half-century since Skumanich (Baliunas et al. 1995; Hall 2008).

The ability to probe the properties of magnetic active regions in photospheres has come into focus more recently, due in part to the now widespread availability of space-based photometry from NASA’s *Kepler*, *K2*, and *TESS* missions. Space-based photometry is precise enough to measure rotation periods accurately even for relatively inactive stars, enabling photometric detections of flux variations that were previously very difficult or impossible to measure from the ground.

The *Kepler* mission observed 150,000 stars just above the galactic plane (Borucki et al. 2010, 2011). McQuillan et al. (2014) found that most stars in the *Kepler* field are consistent

with a gyrochronological age of 4.5 Gyr. There was also a young cluster in the original *Kepler* field, NGC 6811 (1 Gyr; Curtis et al. 2019a). Conforming to new hardware constraints, the following *K2* mission targeted 400,000 stars in the ecliptic plane (Howell et al. 2014), which measured photometry on stars in several clusters of various ages including Upper Scorpius (10 Myr; Pecaú & Mamajek 2016), Praesepe (650 Myr; Douglas et al. 2017), and M67 (4 Gyr; Önehag et al. 2011; Barnes et al. 2016). The *TESS* mission covers 85% of the sky and collects photometry on the brightest stars (Ricker et al. 2014), including stars in several young associations including the Upper Centaurus Lupus (UCL) association (16 Myr; Pecaú & Mamajek 2016), and the Pisces–Eridanus (Psc–Eri) stream (120 Myr; Curtis et al. 2019b).

The wealth of precision photometry available for stars of different ages, as well as precise cluster membership catalogs via *Gaia* observations (Gaia Collaboration et al. 2018), makes it possible to investigate how spot coverage varies as stars age. There is a rich history of attempting to invert photometry of active stars to recover stellar surface intensity maps (see review by Lanza 2016). In general these techniques suffer from many degeneracies; a single light curve can be reproduced by a wide variety of spot models.

In this work, we will make a few critical assumptions to overcome these degeneracies and determine starspot coverages accurately. These assumptions are: (1) that stars of similar age, mass, and rotation period should have similar spot distributions; and (2) the inclination angles of stars are nearly randomly distributed as observed from Earth. If these assumptions are true, then an ensemble of light curves of stars in a young cluster can be used to constrain their spot distributions. One can imagine that photometric surveys of young clusters are essentially observing the same star at many different inclinations, allowing us to marginalize over the unknown inclinations of the individual stars if we model their light curves as a population. A similar hypothesis was used by Jackson & Jeffries (2013).

Table 1
Smoothed Amplitudes and Rotation Periods for All Targets Considered in This Work

Name	Assoc.	Period (day)	Smoothed Amplitude
G 132-51 B	Upper Sco	1.73	0.0394
HIP 6276	Upper Sco	2.73	0.0311
G 269-153 A	Upper Sco	2.40	0.0904
G 269-153 B	Upper Sco	1.77	0.0712
G 269-153 C	Upper Sco	2.43	0.0251
HS Psc	Upper Sco	3.85	0.0666
BD+37 604 Aab	Upper Sco	4.99	0.1422
41 Ari AB	Upper Sco	10.56	0.0737
IS Eri	Upper Sco	5.39	0.1365
HIP 14809	Upper Sco	2.23	0.0176
HIP 14807	Upper Sco	5.33	0.0663
V577 Per A	Upper Sco	2.25	0.0377
V577 Per B	Upper Sco	1.52	0.0506
HIP 17695	Upper Sco	5.84	0.0642
⋮	⋮	⋮	⋮

(This table is available in its entirety in machine-readable form.)

We devise a method for inverting an ensemble of light curves to measure spot coverage as a function of stellar age. In Section 2, we describe several samples of stars sourced from *Kepler*, *K2*, and *TESS* photometry. In Section 3, we outline an efficient algorithm for calculating the rotational modulations of many spotted stars, for comparison with the *Kepler*, *K2*, and *TESS* photometry of young stars. In Section 4 we sample the approximate posterior distributions for the spot coverages of stars in each young association using approximate Bayesian computation (ABC). In Section 5 we discuss the implications for stellar dynamos and exoplanet radii.

2. Stellar Samples

In the present work we limit our analyses to 531 F, G, and K stars. FGK stars likely have fundamentally different dynamos of magnetic activity than M stars, which become fully convective at low masses. For this reason, it may be plausible that FGK stars behave similar to the Sun, whereas M dwarfs quite likely have very different expressions of surface magnetic activity. Also, FGK stars have clearly distinct motions in the observational parameter space, which we will explore in this work, while their M-dwarf siblings often have rapid rotation periods even for older clusters. In this analysis, in which we seek to find a relationship between spot coverage and age, we therefore restrict ourselves to the “solar-type” FGK stars.

2.1. Smoothed Amplitudes

In this section we define what we call the “smoothed amplitude” of each light curve (see Table 1). This quantity was first published by Douglas et al. (2017) for Praesepe members. The smoothed amplitude is the difference between the maximum and minimum flux after the light curve has been phase folded and smoothed with a Gaussian kernel.

2.2. Upper Scorpius (USCO): K2

USCO is a 10 ± 2 Myr old part of the nearby Scorpius–Centaurus (Sco-Cen) star-forming region (Pecaut & Mamajek 2016). We queried for *K2* photometry from FGK members of

the young association listed by Gagné et al. (2018), and found 19 sources. We measure the stellar rotation period for each star by estimating the peak power in the Lomb–Scargle periodogram (Lomb 1976; Press & Rybicki 1989). We then phase fold each light curve on the best period, smooth the light curve with a Gaussian kernel of width 50 cadences, and report smoothed amplitudes. We visually inspected each light curve for hints of binarity in the periodogram (multiple, non-aliased periods), and discarded any possible binaries and stars with ambiguous rotation periods.

2.3. UCL: TESS

UCL is a 16 ± 2 Myr old part of the nearby Sco-Cen star-forming region (Pecaut & Mamajek 2016). We queried for *TESS* photometry of sources listed as UCL members by Gagné et al. (2018), and found 34 sources with *TESS* Input Catalog masses $M > 0.6M_{\odot}$ in the full-frame images (FFIs). We query the FFI database for a square region 10 pixels per side, centered on the coordinates of each UCL member. We subtracted the median flux in a 3 pixel radius circular aperture from each FFI, and remove a quadratic trend from each FFI light curve. As in the previous section, for each light curve, we measure the stellar rotation period for each star by estimating the peak power in the Lomb–Scargle periodogram, limiting the maximum period to half of the *TESS* sector duration. We phase fold each light curve on the best period, smooth the light curve with a Gaussian kernel of width 50 cadences, and report the smoothed amplitude. Again, we visually inspected each light curve for signs of binarity in the periodogram, and discarded any possible binaries. See Figure 1 for a visual representation of this process.

2.4. Psc-Eri: TESS

Psc-Eri is a 120 Myr old stellar stream extending 120° across the sky (Meingast et al. 2019). We followed a similar procedure to the previous subsection to produce light curves for each of 100 FGK targets which were identified as members of the Psc-Eri stream by Curtis et al. (2019b). In addition to using their membership list, we also used the rotation periods reported by Curtis et al. (2019b), and simply measured the smoothed amplitudes of each light curve after phase folding the light curve and smoothing with a Gaussian kernel with width 100 cadences.

2.5. Praesepe: K2

Praesepe is a well-studied, nearby, 650 Myr old cluster. Douglas et al. (2017) measured the amplitudes of rotational modulation of many apparently single stars in Praesepe with *K2*. Here we will focus on stars that are not classified as binaries or blends. The authors calculated “smoothed amplitudes” (which are reported as semi-amplitudes) of the rotational modulation for each star, in which the maximum and minimum flux are measured in smoothed, phase-folded light curves. We adopt the authors’ smoothed amplitudes and rotation periods without modification for 220 FGK stars in Praesepe.

2.6. NGC 6811: Kepler

NGC 6811 is a 1 Gyr old cluster in the *Kepler* field (Meibom et al. 2011). Curtis et al. (2019a) found what they called a temporary epoch of stalled spin-down for low-mass stars in

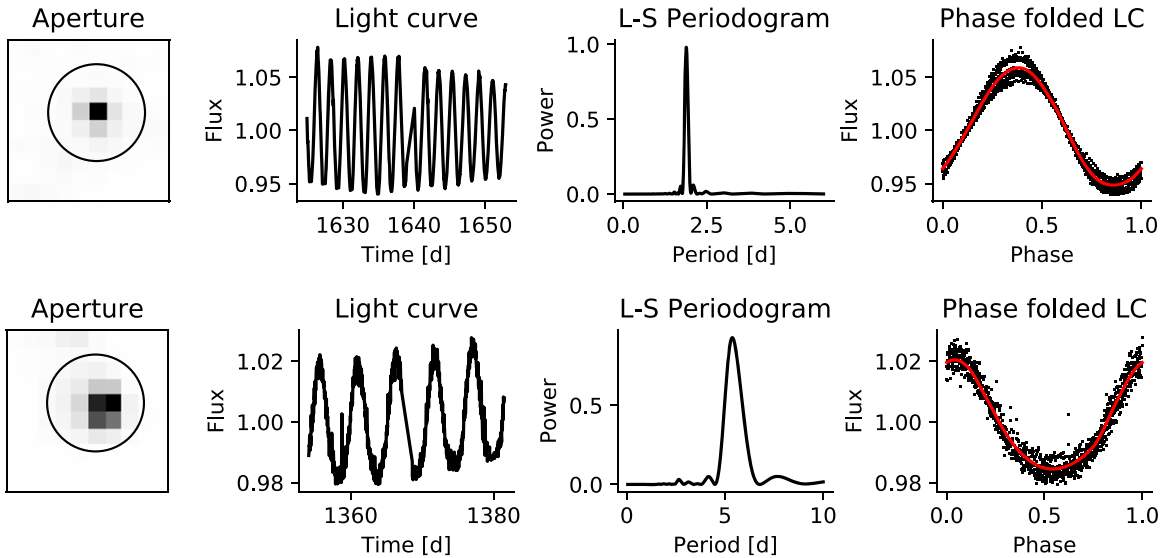


Figure 1. Top row: *TESS* FFI photometry of HD 326277, a member of the 16 Myr-old UCL association. We measure the flux in a 3 pixel radius circular aperture centered on the stellar coordinates, measure the rotation period with the Lomb–Scargle periodogram, and phase fold the light curve on the rotation period to measure the “smoothed amplitude” of the light curve, which is simply the peak-to-trough amplitude of the red curve on the right. Second row: same measurements as above for *Gaia* DR2 4984094970441940864, a member of the Psc-Eri stream (120 Myr). Note that the rotation period is slower and the smoothed amplitude is smaller than HD 326277.

NGC 6811. We use the Curtis et al. (2019a) membership list and rotation periods to build a sample of 167 FGK stars in NGC 6811, and measure smoothed amplitudes from the Pre-search Data Conditioning Simple Aperture Photometry (PDCSAP) fluxes for each star in *Kepler* Quarter 2 using a Gaussian kernel with width 100 cadences. We select only the second quarter of *Kepler* observations to more closely approximate the variability on timescales similar to the *K2* and *TESS* observations; including the full *Kepler* light curve tends to average over many spot evolutions and decrease smoothed amplitudes.

2.7. M67: K2

M67 is a 4.2 ± 0.2 Gyr old cluster in *K2* Campaign 5 (Gonzalez 2016a, 2016b). We use the cluster membership and rotation periods for 96 stars listed in Gonzalez (2016b; which are in good agreement with the periods of Barnes et al. 2016), and measure smoothed amplitudes from the PDCSAP fluxes for each star using a Gaussian kernel with width 250 cadences.

2.8. Trends with Rotation Period and Age

Figure 2 shows a trend in the observable properties of the light curves: there is an anti-correlation between the typical rotation periods of stars in each cluster and the smoothed amplitude of the light curves. One useful perspective encoded in this plot has to do with the axisymmetry of the starspot distributions. If a star has several starspots which are distributed uniformly in longitude, the rotational modulation amplitude will be relatively small; whereas if spots are concentrated into a small region on one stellar hemisphere, the rotational modulation amplitude will be relatively large. Young stars have short rotation periods and large smoothed amplitudes, corresponding to significant concentrations of dark spots, or significant deviations from uniformly distributed spots. As stars age they drift toward the upper left of the plot (following the direction of the silver arrow); their rotation

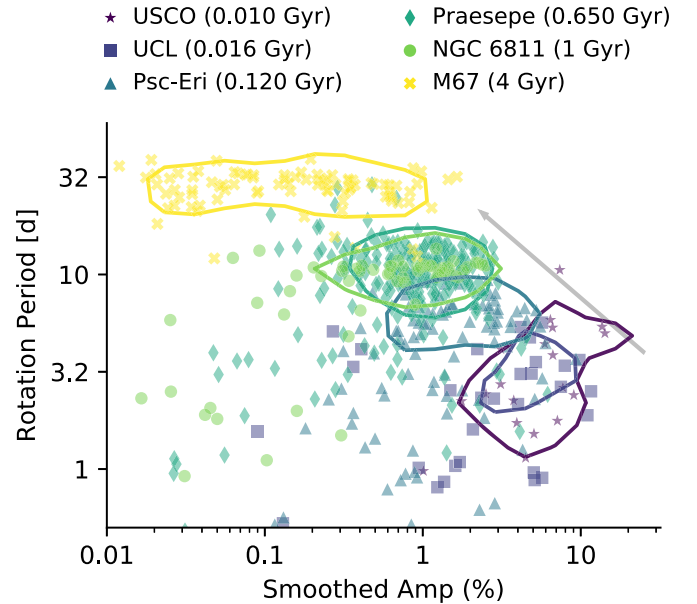


Figure 2. Rotation periods as a function of smoothed amplitudes for the FGK stellar samples defined in Section 2. Smoothed contours are drawn around stars in each sample to guide the eye. (These contours are drawn by generating a 2D histogram of the stellar samples, smoothing it with a Gaussian, and selecting a cutoff level for drawing the contour.) The youngest stars fall in the bottom-right of the plot, corresponding to large longitudinal asymmetries in spot distributions and short rotation periods, while the older stars have smaller smoothed amplitudes, i.e., more uniform longitudinal starspot distributions, and longer rotation periods. Figure 3 shows the same observations with an age axis. The spread in the smoothed amplitude axis may be due to activity cycle phase, stellar inclination, or a combination of the two.

periods increase and their smoothed amplitudes decrease, or their spots become distributed more uniformly.

Figure 3 shows another view of the stellar samples in Figure 2, demonstrating the decay of the smoothed amplitude as a function of cluster age. The linear regression trend line (gray) indicates that smoothed amplitudes of light curves

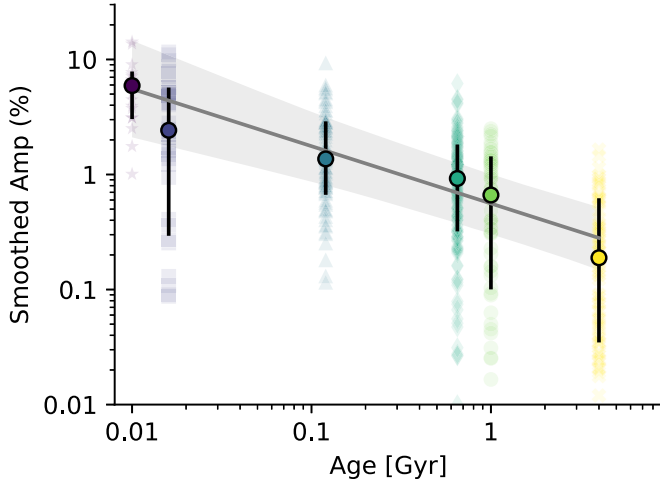


Figure 3. Smoothed amplitudes of the light curves of the FGK stars in each association as a function of age. The colors and symbol shapes correspond to the legend in Figure 2.

generally decline with increasing stellar age, as

$$\text{Smoothed Amplitude [\%]} = \alpha t^m, \quad (1)$$

where and $\alpha = 0.56^{+1.00}_{-0.31}$ and $m = -0.498 \pm 0.166$.

This power-law index m is remarkably close to the $t^{-1/2}$ decline in chromospheric emission with age discovered by Skumanich (1972). Perhaps this result suggests there may be a simple relationship between the area in chromospherically active regions and the area in starspots, causing this simple metric for the spot coverage, the smoothed amplitudes, to have the same age dependence as the chromospheric emission index (such relations already exist for magnetic field strength and Ca emission, for example, Schrijver et al. 1989).

3. Forward Modeling Ensembles of Light Curves

We now seek to essentially re-calibrate the vertical axis in Figure 3 by mapping smoothed-amplitude distributions onto hemispheric spot covering fractions, f_S . In order to do this, we must first devise a technique for simulating photometry of an ensemble of rotating stars.

3.1. Vectorized Ensemble Light-curve Generation

We simulate ensembles of light curves of stars through a full rotation and measure their smoothed amplitudes using *fleck*.¹ *Fleck* is a pure Python software package that simulates starspots as circular dark regions on the surfaces of rotating stars, accounting for foreshortening toward the limb, and limb darkening, which is an efficient, vectorized iteration of earlier codes used in Morris et al. (2018, 2019). The *fleck* algorithm is outlined as follows: suppose we have N stars, each with M starspots, distributed randomly above maximum latitudes ℓ_{\max} , observed at N inclinations i_* (one unique inclination per star), observed at O phases throughout a full rotation $\phi \sim \mathcal{U}(0, 90^\circ)$.

We initialize each star such that its rotation axis is aligned with the \hat{z} axis, and set the observer at $x \rightarrow \infty$, viewing down the \hat{x} axis toward the origin.

We define the rotation matrices about the \hat{y} and \hat{z} axes for a rotation by angle θ :

$$\mathbf{R}_y(\theta) = \begin{bmatrix} \cos \theta & 0 & \sin \theta \\ 0 & 1 & 0 \\ -\sin \theta & 0 & \cos \theta \end{bmatrix} \quad (2)$$

$$\mathbf{R}_z(\theta) = \begin{bmatrix} \cos \theta & -\sin \theta & 0 \\ \sin \theta & \cos \theta & 0 \\ 0 & 0 & 1 \end{bmatrix}. \quad (3)$$

We begin with the matrix of starspot positions in Cartesian coordinates \mathbf{C}_i ,

$$\mathbf{C}_i = \begin{bmatrix} x_1 & y_1 & z_1 \\ x_2 & y_2 & z_2 \\ \vdots & \vdots & \vdots \\ x_M & y_M & z_M \end{bmatrix},$$

for $i = 1$ to N with shape $(3, M)$, which we collect into the array \mathbf{S}

$$\mathbf{S} = [\mathbf{C}_1, \mathbf{C}_2, \dots, \mathbf{C}_N],$$

of shape $(3, M, N)$. We rotate the starspot positions through each angle in ϕ_j for $j = 1$ to O by multiplying \mathbf{S} by the rotation array

$$\mathbf{R}_z = [[\mathbf{R}_z(\phi_1)], [\mathbf{R}_z(\phi_2)], \dots, [\mathbf{R}_z(\phi_O)]],$$

with shape $(O, 1, 1, 3, 3)$. Using Einstein notation, we transform the Cartesian coordinates array \mathbf{C} with

$$\mathbf{R}_{z[lm \dots]ij} \mathbf{S}^{j[lm \dots]} = \mathbf{S}'_{i[lm \dots]} \quad (4)$$

to produce an array with shape $(3, O, M, N)$, where lm indicates an optional additional set of dimensions. Then after each star has been rotated about its rotation axis in \hat{z} , we rotate each star about the \hat{y} axis to represent the stellar inclinations $i_{*,k}$ for $k = 1$ to N , using the rotation array

$$\mathbf{R}_y = [\mathbf{R}_y(i_{*,1}), \mathbf{R}_y(i_{*,2}), \dots, \mathbf{R}_y(i_{*,N})]$$

with shape $(N, 3, 3)$, by doing

$$\mathbf{R}_{y[lm \dots]ij} \mathbf{S}'^{j[lm \dots]} = \mathbf{S}''_{i[lm \dots]}, \quad (5)$$

which produces another array of shape $(3, O, M, N)$. Now we extract the second and third axes of the first dimension, which correspond to the y and z (sky-plane) coordinates, and compute the radial position of the starspot $\rho = \sqrt{y^2 + z^2}$, where ρ has shape (O, M, N) . We now mask the array so that any spots with $x < 0$ are masked from further computations, as these spots will not be visible to the observer. We use ρ to compute the quadratic limb darkening

$$I(\rho) = \frac{1}{\pi} \frac{1 - u_1(1 - \mu) - u_2(1 - \mu)^2}{1 - u_1/3 - u_2/6} \quad (6)$$

for $\mu = \sqrt{1 - \rho^2}$. We compute the flux missing due to starspots of radii \mathbf{R}_{spot} , which has shape (M, N) :

$$F_{\text{spots}} = \pi \mathbf{R}_{\text{spot}}^2 (1 - c) \frac{I(r)}{I(0)} \sqrt{1 - \rho^2}. \quad (7)$$

¹ <https://github.com/bmorris3/fleck>

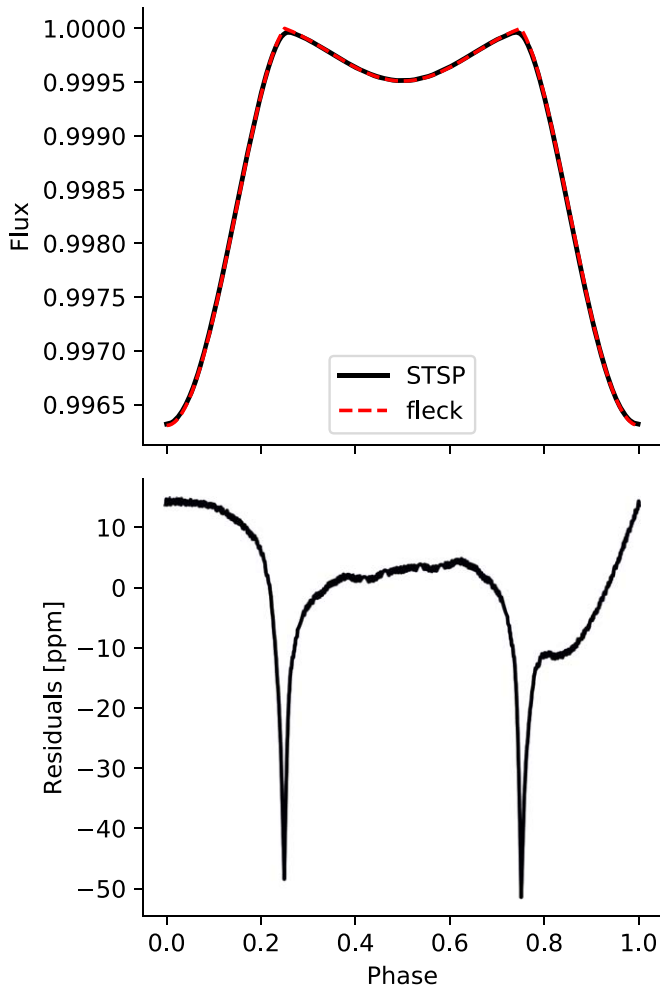


Figure 4. Comparison between the approximate fleck and the more accurate STSP starspot models, for spots of size $R_{\text{spot}}/R_{\star} = 0.1$. The agreement between models is on the order of the noise in *Kepler* photometry, so we deem the approximations in fleck to be valid for the space-based photometry considered here.

The unspotted flux of the star is

$$F_{\text{unspotted}} = \int_0^R 2\pi r I(r) dr, \quad (8)$$

so the spotted flux is

$$F_{\text{spotted}} = 1 - \frac{F_{\text{spots,ijk}} F_{\text{spots}}^{\text{ik}}}{F_{\text{unspotted}}}. \quad (9)$$

3.2. Limitations of the Model

The model presented above works best for spots that are small. The array masking step for $x < 0$ does not account for the change in stellar flux due to large starspots that straddle the limb of the star. Large starspots also have differential limb darkening across their extent, which is not computed by fleck.

Comparison with STSP² is shown in Figure 4. The models reproduce consistent rotational light curves at the 50 ppm level—similar to the *Kepler* noise floor on 1 hr timescales for bright stars (Borucki et al. 2011; Christiansen et al. 2012). The maximum divergence between models occurs when the spots

are near the limb, where STSP accounts for the spot that straddles the limb and fleck does not. The differences between the models are small compared to the uncertainties in flux of the *K2* photometry, for instance.

4. ABC

Fleck makes it simple to generate new simulated data sets of light curves and their corresponding smoothed-amplitude distributions, as shown in Figure 5. It is difficult, however, to write down the likelihood of reproducing the observed smoothed amplitudes given a set of spot parameters. When it is straightforward to compute simulated data sets for comparison with observations, but it is difficult to write down the likelihood, ABC is a practical tool for sampling from the posterior distributions of parameters (Sunnåker et al. 2013; Akeret et al. 2015; Lintusaari et al. 2016; Sisson et al. 2018).

In order to find the most likely spot covering fraction f_S given an observed smoothed-amplitude distribution, we explore the spot radius–position–contrast parameter space using ABC. ABC allows us to approximate the posterior PDFs of the spot radius, position, and contrast parameters, to ultimately probe which spot covering fractions are compatible with the observations.

The stellar rotational modulation forward-model built with fleck has three free parameters $\theta^* = \{\ell_{\text{max}}, R_{\text{spot}}/R_{\text{star}}, c\}$, the minimum spot latitude above which spots are randomly distributed ℓ_{max} , the spot radius $R_{\text{spot}}/R_{\text{star}}$, and the spot contrast c which varies on $[0, 1]$ where $c \rightarrow 0$ approaches perfectly dark spots and $c \rightarrow 1$ are spots with the same intensity as the photosphere. We assign uniform bounded prior probability distributions $\mathcal{U}(0, 90^\circ)$, $\mathcal{U}(0, 1)$, $\mathcal{U}(0, 1)$, respectively. We use fleck to generate thousands of light curves of stars observed at random inclinations, producing one trial smoothed-amplitude distribution per θ^* .

We construct a simple rejection sampling algorithm which operates as follows: (1) perturb the previous step to propose a new set of parameters θ^* drawn from the prior; (2) use fleck to compute the smoothed-amplitude distribution for a large sample of stars, (3) for use as a summary statistic, we compute the two-sample Anderson–Darling statistic A^2 for comparing how close the trial smoothed-amplitude distribution is to the observed one (Anderson & Darling 1952; Scholz & Stephens 1987, see discussion in Appendix 6); (4) if $A^2 < A_{\text{crit}}^2$, we accept the proposed step and add it to our chain; (5) go back to step (1), and repeat. We select $A_{\text{crit}}^2 = 0$, not far from the minimum value of the Anderson–Darling statistic $A_{\text{min}}^2 \sim -1.3$.

The approximate posterior distributions produced by ABC should approach the true posterior distributions in the limit that $A_{\text{crit}}^2 \rightarrow A_{\text{min}}^2$, provided that the Anderson–Darling statistic is a sufficient statistic. In practice it is difficult to prove that a statistic is sufficient, so we note that the posterior distributions shown here are valid given the hypothesis that the Anderson–Darling statistic is a sufficient one.

The posterior distributions from the ABC analysis illustrate the three-way degeneracy between starspot latitudes, radii, and contrasts for stars with unknown inclinations. For a fixed number of spots, small spots spread randomly over all latitudes generate rotational modulations similar to larger spots concentrated near the poles. Similarly, small spots with extreme intensity contrasts ($c \rightarrow 0$) reproduce similar rotational modulations to larger spots with less extreme spot contrasts

² <https://github.com/lesliehebb/STSP>

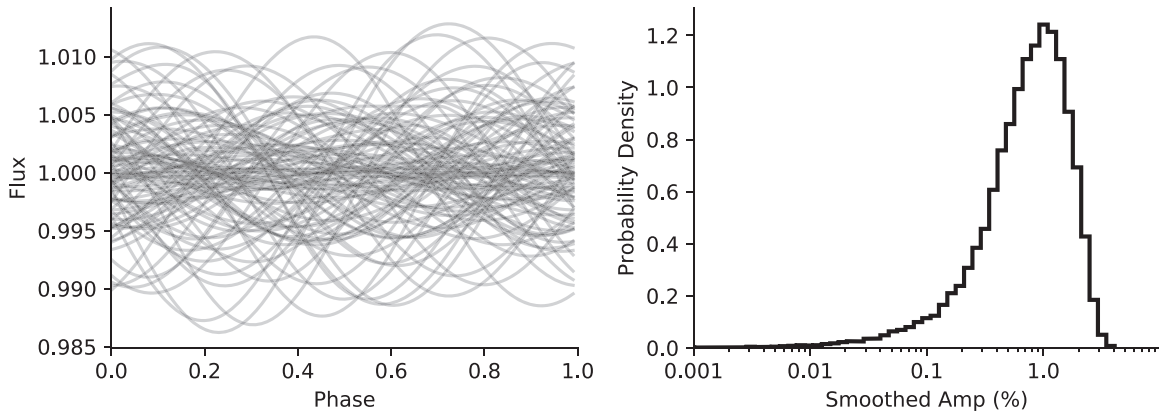


Figure 5. Outputs of the fleck algorithm, which produces light curves throughout stellar rotations (left), allowing us to measure the difference between the maximum and minimum fluxes for large ensembles of light curves (right). We compare the amplitude distribution of the simulated light curves on the right to the observed distributions of smoothed amplitudes for cluster stars using ABC.

($c \rightarrow 1$). This exercise is a demonstration of why it is so difficult to invert light curves of rotational modulation and recover unique starspot properties—a wide range of spot parameters can produce similar light curves.

Figure 6 shows the simulated smoothed-amplitude distributions (gray histograms) with spot parameters drawn randomly from the posterior distributions, compared with the observed smoothed-amplitude distribution for stars in each association (colored histograms). This figure illustrates how the ABC algorithm minimized the Anderson–Darling statistic between the simulated and observed smoothed-amplitude distributions. Most simulated and observed distributions are statistically indistinguishable according to the Anderson–Darling statistic.

The poorest “fit” is M67, the oldest cluster, for which the simulations produce a more strongly peaked smoothed-amplitude distribution near 0.5%. The lack of a peak in the observed smoothed-amplitude distribution for M67 is likely real; observational bias in favor of detecting large amplitude variability would cause a peak at large smoothed amplitudes. The lack of a peak in the smoothed-amplitude distribution may be a hint that the spin axes of the stars in M67 are not randomly distributed (see further discussion in Section 5.2.5).

The approximate posterior distributions for the total spot coverage are shown in Figure 7. The ABC technique constrains the spot coverage for each stellar sample to between $0.05 < f_S < 0.2$ for the youngest stars (at 10 Myr in USCO), and $0.002 < f_S < 0.02$ for the oldest stars (at 4 Gyr in M67).

5. Discussion

5.1. A Relation between Starspot Coverage and Stellar Age

The relationship between starspot coverage and age can be deduced from the slope and intercept in the right panel of Figure 7. We find the hemispheric starspot covering fraction f_S is related to the stellar age t in Gyr by the simple relation

$$f_S \approx at^n, \quad (10)$$

where $a = 0.014^{+0.022}_{-0.008}$ and $n = -0.37 \pm 0.16$. The power-law index n is statistically consistent with the approximate inverse square root relation between chromospheric activity and stellar age by Skumanich (1972).

One must take care not to infer upper or lower limits to the spotted coverage of individual stars of a given age from Equation (10). The light-curve ensemble modeling technique

constrains a typical spot coverage for stars in each sample, and outliers are likely to exist that will not fall neatly within the confidence intervals of Equation (10).

LkCa 4, for example, is a weak-lined T Tauri star in the Taurus Molecular Cloud (< 10 Myr; Kenyon & Hartmann 1995). High-resolution near-infrared IGRINS spectra from Gully-Santiago et al. (2017) constrained the star’s spot coverage to $f_S \sim 0.8$. The authors argue that such a large coverage by dark regions challenges our notion of “spot coverage,” since the majority of the stellar photosphere emits at a cooler temperature than its spectral type (Pettersen et al. 1992). The ensemble light-curve modeling technique assumed three starspots that cover a minority of the stellar surface, so the results (Equation (10)) should not be applied to stars covered in mostly cool regions, like LkCa 4.

5.1.1. Relating Smoothed Amplitude to Spot Coverage

Given that we have established a relationship between spot coverage and age and smoothed amplitude and age, we can infer the relationship between spot coverage and smoothed amplitudes,

$$f_S = a \left(\frac{\text{Sm Amp} [\%]}{\alpha} \right)^{n/m}, \quad (11)$$

or approximately

$$f_S \sim 0.02 \times (\text{Sm Amp} [\%])^{0.74}. \quad (12)$$

We caution users of this formula that it only describes how ensembles of stars behave on average, and that one should not infer spot coverage for individual stars directly from light-curve amplitudes, as the light-curve amplitude is degenerate with the stellar inclination and spot contrast.

5.2. Second-order Effects

In this subsection we discuss several factors that may have small but significant effects on the conclusions drawn from the ABC analysis.

5.2.1. Comparing Rotational Modulation across Bandpasses

One difficulty in comparing photometry across two telescopes is that *Kepler*, *TESS*, and *Gaia* all have a slightly different bandpasses. Fortunately, the effect of the slightly

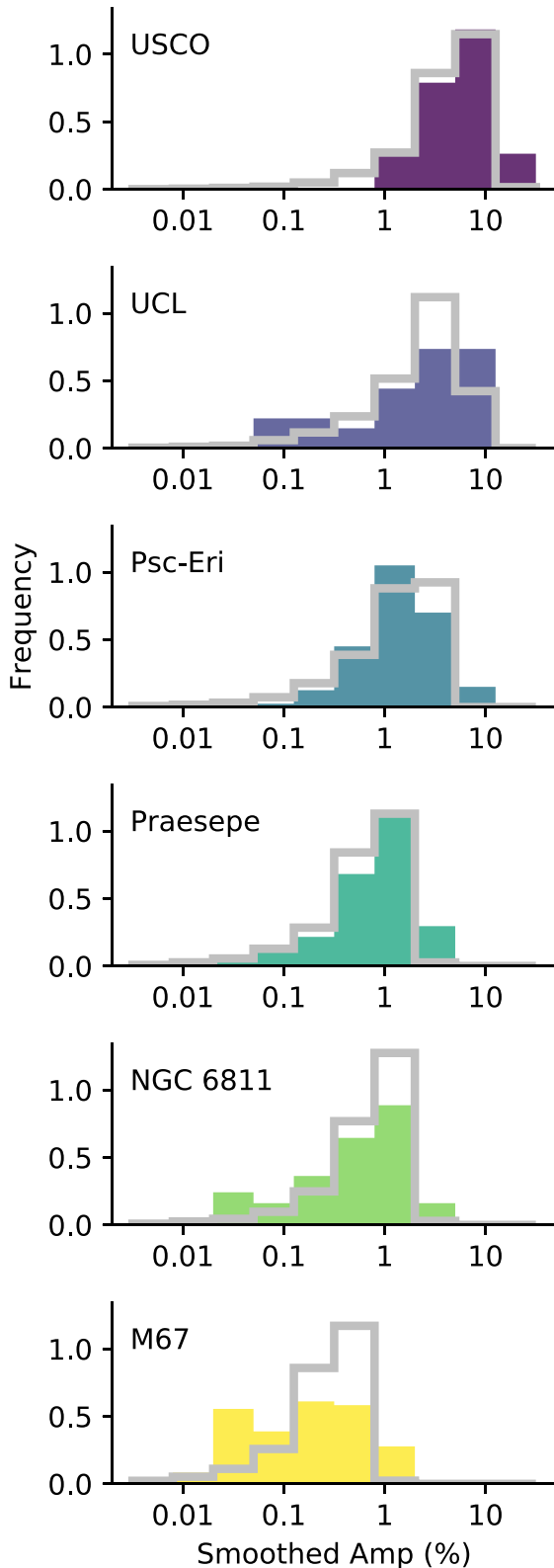


Figure 6. Observed smoothed light-curve amplitude distributions (colored histograms) compared with simulated smoothed-amplitude distributions (gray) drawn from the posterior distributions for the spot parameters from the ABC technique with fleck. The goal of the ABC technique is to search for starspot parameters that produce simulated smoothed-amplitude distributions that are statistically indistinguishable from the observations.

different bandpasses on the scale of rotational modulation is small (see Figure 2 of Morris et al. 2018). Future catalogs of photometry from the *Gaia* mission may also prove useful in measuring the photometric variability of young stars due to starspots.

5.2.2. Activity Cycles

Magnetic activity cycles with timescales of years to decades will be a source of imprecision in the spot distribution analysis. Stars observed near activity minima will have smaller smoothed amplitudes than identical stars observed near activity maxima, creating a distribution in smoothed-amplitude space for even a single star observed through time. Furthermore, the properties of the activity cycle vary with stellar age; Baliunas et al. (1995) found that younger, rapidly rotating G and K stars have more stochastic variations when compared with older, more slowly rotating stars with smooth, cyclic activity patterns.

In this work we assume that by observing samples of tens to hundreds of stars at each age, we are observing stars at a variety of activity cycle phases. In this sense, we may be implicitly marginalizing over the latent activity cycle phase variable within each stellar subsample. Some stars will be observed near minimum and have smaller light-curve amplitudes, while others will be observed near maximum and have larger amplitudes. The broad confidence interval shown in Figure 7 may therefore already account for some of the apparent broadening in the f_S distributions of stars due to activity cycles.

5.2.3. Metallicity and Magnetic Activity Cycles

It has been claimed that metallicity may affect the photometric variability of stars throughout their magnetic activity cycles. Karoff et al. (2018) measured the photometric variations of HD 173701, a star with twice the solar metallicity, and found that its variability amplitude is significantly larger than solar. When more photometry and cluster membership catalogs become available, it may be necessary to add a third dimension to the analysis of spot coverage as a function of stellar age, which parameterizes variation in spot coverage with stellar metallicity.

5.2.4. Starspot Evolution

Giles et al. (2017) showed that starspots have longer lifetimes on cooler stars. When one phase folds the light curve of a solar-mass star, the light-curve amplitude may vary strongly as a function of the duration of the bin over which the light curve is phase folded. Smaller duration bins will match the comparatively short lifetimes of starspots on Sun-like stars (\lesssim months), giving accurate representations of the true light-curve amplitude. Larger duration bins, like the four-year *Kepler* light curves of NGC 6811, will integrate over several spot evolutions and therefore may dilute the true amplitude of the light-curve variation. For this reason, we used a single *Kepler* quarter rather than the full *Kepler* light curves for NGC 6811.

5.2.5. Stellar Inclination Distribution

We have assumed that spin axes of stars are distributed randomly. Spins of stars in old open clusters may be preferentially

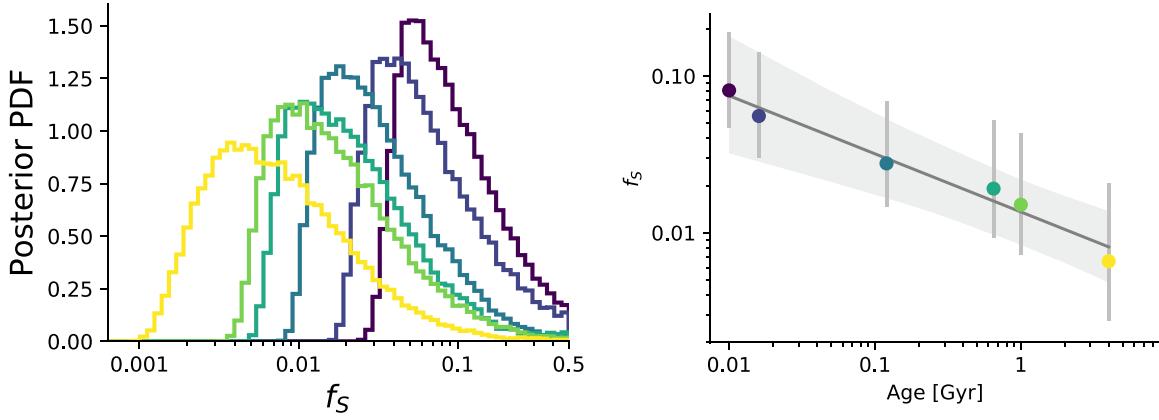


Figure 7. Approximate posterior distributions for the total spot coverage f_s for stars in each association. Colors correspond to the legend in Figure 2. As stars age (from purple through yellow), the most likely spot coverage f_s decreases from 8% at 10 Myr (USCO, purple) down to 0.8% at 4 Gyr (M67, yellow). Colors correspond to the legend in Figure 2.

Table 2
Spot Coverage on Planet-hosting Stars

Star	Spectral Type	Photometry Source	Age (Myr)	f_s	
				Predicted	Measured
V1298 Tau	K0	<i>K2</i>	23 ± 4 (a)	$0.05^{+0.06}_{-0.02}$	$0.09^{+0.01}_{-0.02}$
DS Tuc A	G6V	<i>TESS</i>	45 ± 4 (b)	$0.04^{+0.04}_{-0.02}$	$0.071^{+0.003}_{-0.003}$
Qatar-4	K1V	<i>TESS</i>	170 ± 10 (c)	$0.03^{+0.02}_{-0.01}$	$0.030^{+0.009}_{-0.006}$
Kepler-411	K2V	<i>Kepler</i>	212 ± 31 (d)	$0.02^{+0.02}_{-0.01}$	$0.017^{+0.003}_{-0.002}$
WASP-52	K2V	<i>HST</i> /WFC3	400^{+300}_{-200} (e)	$0.01 - 0.04$	0.05 ± 0.01^h
Kepler-289	G0V	<i>Kepler</i>	650 ± 440 (f)	$0.015^{+0.009}_{-0.006}$	$0.031^{+0.002}_{-0.005}$
EPIC 247589423	K5.5	<i>K2</i>	687 ± 063 (j)	$0.014^{+0.009}_{-0.006}$	$0.0066^{+0.0017}_{-0.0016}$
K2-100	G0V	<i>K2</i>	790 ± 30 (k)	$0.014^{+0.009}_{-0.006}$	$0.032^{+0.003}_{-0.001}$
K2-101	K2V	<i>K2</i>	790 ± 30 (k)	$0.014^{+0.009}_{-0.006}$	$0.035^{+0.0004}_{-0.003}$
Kepler-21	F6V	<i>Kepler</i>	2600 ± 160 (l)	$0.009^{+0.006}_{-0.003}$	<0.001
Kepler-50	F7V	<i>Kepler</i>	3590^{+780}_{-450} (l)	$0.007^{+0.005}_{-0.003}$	<0.001
Sun	G2V	...	4570 ± 10 (g)	$0.007^{+0.005}_{-0.003}$	$<0.005^i$

Note. Spot coverages f_s “predicted” from the stellar ages (via Equation (10)) compared with “measured” spot coverages from direct modeling of the light curves with fleck (for all targets except WASP-52), and *Hubble Space Telescope* (HST)/WFC3 spot occultation measurements (for WASP-52). Predicted and measured spot coverages are plotted in Figure 9.

References. (a) David et al. (2019a, 2019b), (b) Newton et al. (2019), (c) Alsubai et al. (2017), (d) Sun et al. (2019), (e) Hébrard et al. (2013); Kirk et al. (2016); Bruno et al. (2018), (f) Schmitt et al. (2014), (g) Sonett et al. (1991), (h) Bruno et al. (2019), (i) Morris et al. (2017), (j) Ciardi et al. (2018); Mann et al. (2017), (k) Mann et al. (2017), (l) Silva Aguirre et al. (2015).

aligned with one another (Corsaro et al. 2017; Kovacs 2018), which would introduce yet another set of degenerate parameters into the ABC analysis.

5.3. Comparison with Observations of Planet-hosting Stars

In addition to ensemble light curve modeling, we can also use fleck to directly model the photometry of individual stars. In this section, we fit the fleck model to the light curves of spotted stars with Markov Chain Monte Carlo to validate the spot coverage relation in Equation (10) for stars with precise photometry and ages, listed in Table 2.

As discussed earlier, the positions, radii, and contrasts of starspots are degenerate with one another, making it difficult to extract precise spot properties from the rotational modulation of planet-hosting stars. Thus we make several simplifying assumptions that allow us to fit for the spot coverage on these stars. First, we assume that the stellar inclination is $i_* = 90^\circ$,

which may be a good approximation since each of these systems host (often multiple) transiting exoplanets. Next, we fix the spot contrast to $c = 0.7$; this is compatible with the area-weighted spot coverage of sunspots, the starspot contrasts of HAT-P-11 (Morris et al. 2017), and a valid approximation to the observed spot contrasts of several stars extrapolated into the *Kepler* and *TESS* bandpasses (Morris et al. 2018). We also place a uniform bounded prior on the spot latitudes $|\ell| < 60^\circ$. It is necessary to impose this latitude prior because without it the Markov chains occasionally prefer spots with implausibly large radii, skewing the fits toward large spot coverage; this prior is consistent with solar observations since sunspots are not observed above $\sim 45^\circ$ (Morris et al. 2019). Finally, we also enforce the prior that $0 < R_{\text{spot}}/R_{\text{star}} < 1$, ensuring that the largest spots are still small compared to the stellar radius, to forbid spots with radii several orders of magnitude larger than the largest sunspot groups.

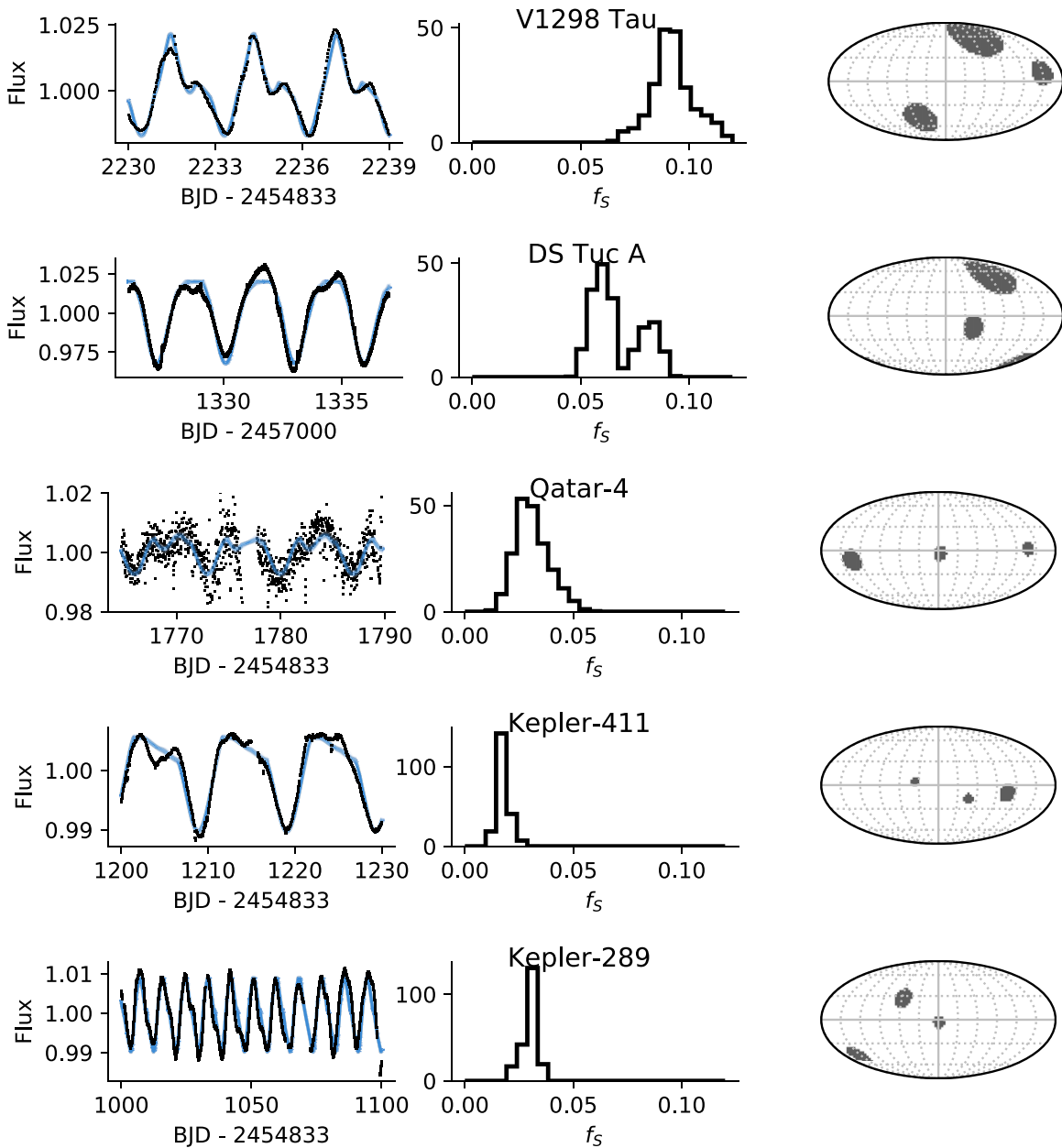


Figure 8. Starspot rotational modulation models generated with fleck (left, blue) for selected portions of observations (left, black); the posterior distributions for the spot coverage (middle); and a single draw from the spot parameter posterior distributions visualized in the Mollweide projection (right). Note that the solutions to the spot latitudes are perfectly degenerate about the equator. Figure continues on next page.

We choose to fix the number of starspots to three in each fit. We find that fitting less than three spots does not accurately reproduce the observed rotational modulation, and fitting additional spots does not significantly improve the fits.

The photometry, maximum-likelihood models, spot coverage posterior distributions, and spot maps are shown in Figure 8. The three-spot model reasonably approximates the rotational modulation in each light curve. Then we compare the posterior distributions for the expected spot coverage inferred from the fleck³ models with the spot coverage estimate from Equation (10) in Figure 9. Most stars fall within the 1σ confidence interval for the predicted spot coverage.

We include an upper limit for the spot coverage of the Sun in Figure 9 using the Mount Wilson Observatory sunspot catalog

(Howard et al. 1984), analyzed in the stellar context by Morris et al. (2017).

Equation (10) tends to overpredict the amplitudes of rotational modulation in the oldest stars: Kepler-21, Kepler-50, and the Sun (Figure 9). Some possible explanations for the overestimation include: (1) cluster stars like those of M67, which are the anchors for the spot coverage relation near 4 Gyr, are more active than field stars like *Kepler-21* and *Kepler-50*; (2) spots are more uniformly distributed on old field stars, diminishing the rotational modulation amplitude; (3) the field stars could have been observed near activity minimum; or (4) we may be viewing *Kepler-21* and *Kepler-50* at low inclinations, producing small light-curve amplitudes. A larger sample of >4 Gyr stars with precise ages and clear rotational modulation is required to determine whether or not a break in the power law near 1 Gyr is justified.

³ github.com/bmorris3/fleck

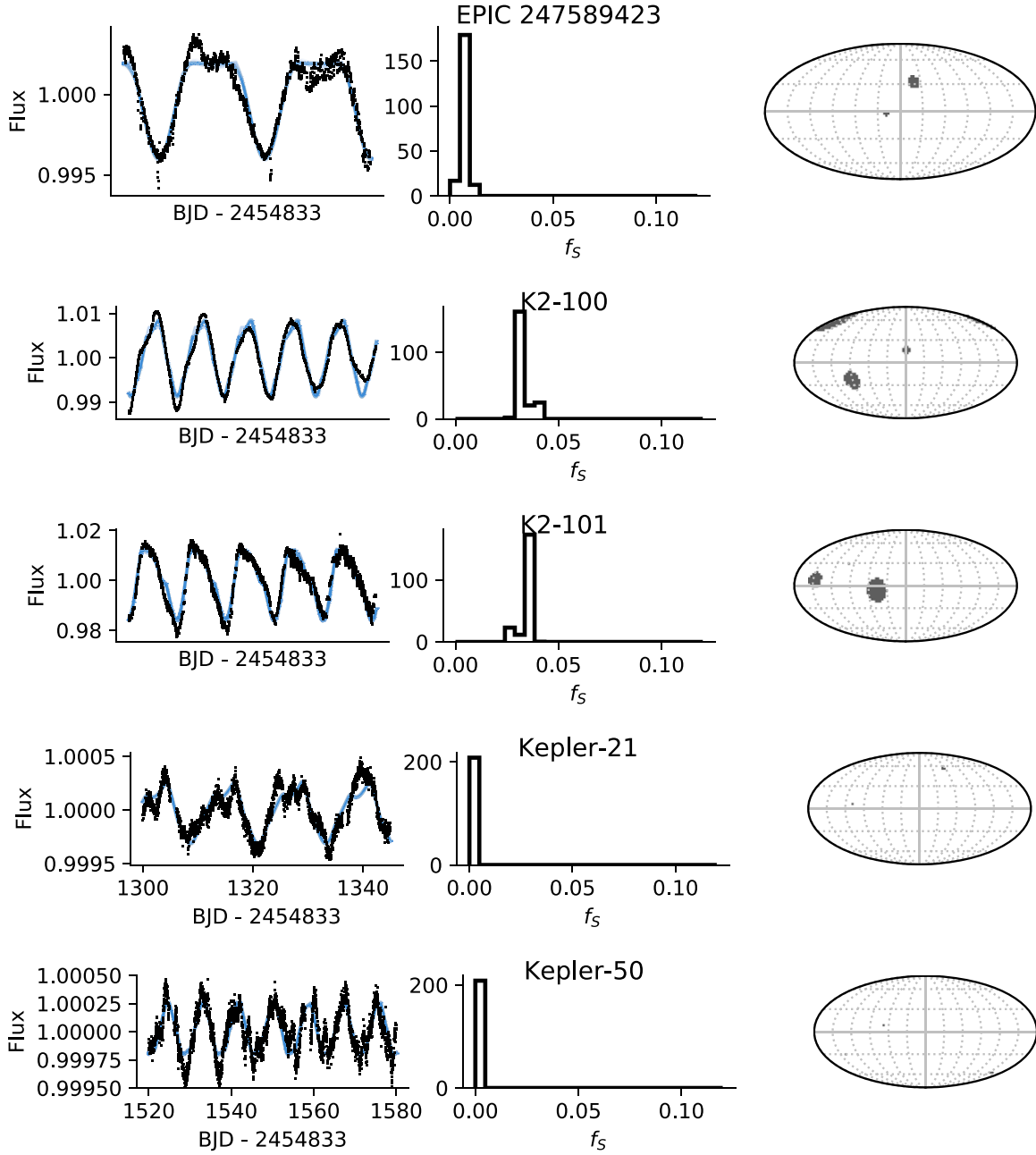


Figure 8. (Continued.)

5.4. Implications for Young Exoplanet Radii

Exoplanet radii are measured from the depths of their transit light curves. Unocculted dark starspots slightly increase the depths of transit light curves, giving the appearance of slightly larger planets. In this section we quantify the extent of exoplanet radius amplification by dark starspots.

The Mandel & Agol (2002) transit model for a uniform source is computed

$$F^e(t) = 1 - \lambda^e(t), \quad (13)$$

where $\lambda^e(t)$ is the fraction of the host star eclipsed. However, this is assuming the eclipsed body is not changing in

brightness. If the host star is changing in brightness, Equation (13) becomes

$$F^e(t) = F_\star(t) - \lambda^e(t), \quad (14)$$

where $F_\star(t)$ is the brightness of the star as a function of time relative to the unspotted stellar flux. In practice, observations of individual transits are often normalized by the out-of-transit flux immediately preceding and following the transit event, so what is observed is

$$F_{\text{obs}}(t) \approx \frac{F_\star(t) - \lambda^e(t)}{F_\star(t)}. \quad (15)$$

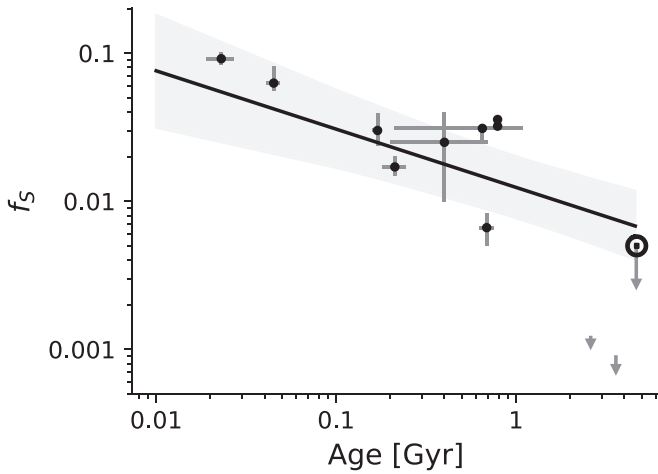


Figure 9. Comparing the posterior spot coverage distributions from direct modeling of light curves of planet-hosting stars in Table 2 with the relation in Equation (10) (black curve, gray 1σ confidence interval). The solar measurement of spot coverage is an upper limit based on the most-spotted observation of the Sun.

For a star with quadratic limb darkening, for example, the maximum flux obscured during the transit event is

$$\lambda_{\max}^e = \left(\frac{R_p}{R_*}\right)^2 \times \frac{1 - u_1(1 - \sqrt{1 - b^2}) - u_2(1 - \sqrt{1 - b^2})^2}{1 - \frac{u_1}{3} - \frac{u_2}{6}}, \quad (16)$$

where b is the impact parameter, so the minimum observed flux during a transit event $F_{\text{obs,min}}$ is

$$F_{\text{obs,min}} \approx 1 - \frac{\lambda_{\max}^e}{F_*(t)}. \quad (17)$$

Since a spotted star has $F_*(t) \leq 1$, it is clear that the transit depth $\delta_{\text{obs}} = \lambda_{\max}^e / F_*$ is amplified by a dimmer, more spotted surface. It is straightforward to compute $F_*(t)$ for spotted stars with fleck, so we can easily compute δ_{obs} given parameters for the planet and starspots.

We simulate a star with three large spots of radius $R_{\text{spot}}/R_* = 0.4$, with stellar inclination $i_* = 90^\circ$, and a planet with $R_p/R_* = 0.1$ at impact parameter $b = 0$ with solar quadratic limb-darkening parameters. This is equivalent to the very large spot coverage $f_s = 0.12$. The results are shown in Figure 10. The transit depth can be amplified by as much as 10% by the modulation due to starspots. This is large enough to be detected given typical observational uncertainties on the radii of small planets orbiting FGK stars, so the variation in transit depth as a function of time is likely an important factor for accurately measuring exoplanet radii orbiting stars with ages $\lesssim 20$ Myr.

6. Summary

We present photometric amplitudes of rotational modulation for 531 F, G, and K stars in six associations ranging in ages from 10 Myr to 4 Gyr. The age and rotation period are anti-correlated with the amplitudes of the light curves, which follows a Skumanich-like spin-down relation with age (Figure 2 and 3). Using the rotational modulation model fleck

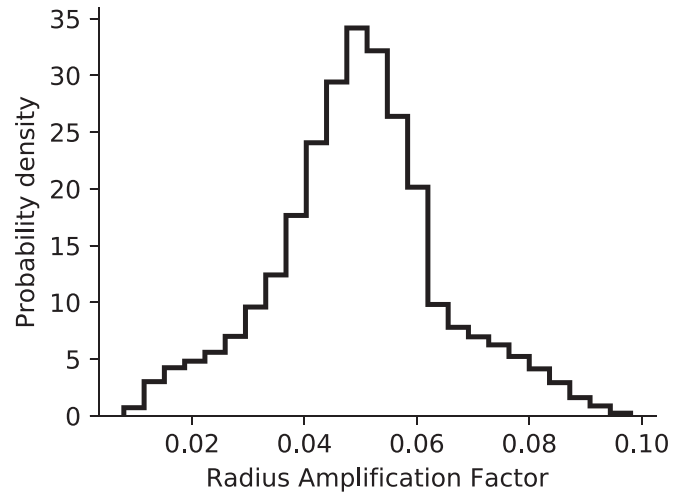


Figure 10. Apparent radius amplification due to transits at different points in the starspot modulation, for a very spotted star with $f_s = 0.12$ and a giant transiting exoplanet. The maximum contamination in the radius measurement due to starspots is about 10% in this extreme case.

(Figure 5), along with an ABC technique (Figure 6), we estimate the spot coverage of stars as a function of age (Figure 7), and find that spot coverage decays like t^n where t is the stellar age in Gyr and $n = -0.37 \pm 0.16$, compatible with a decay of spot coverage like the $t^{-1/2}$ relation discovered by Skumanich (1972).

We measured spot coverages of several planet-hosting stars with precise ages by modeling their rotational modulation (Figure 8), and found good agreement between the measured and predicted spot coverages from the power-law relation (Figure 9 and Table 2).

Based on the spot coverage estimates for young stars, we estimate that variations in the baseline flux of young FGK stars with ages $\lesssim 20$ Myr can cause apparently amplified exoplanet radii by up to 10% (Figure 10).

Jupyter notebooks are available online⁴ which can be used to reproduce this analysis.

We are grateful for insightful conversations with Suzanne Hawley, Michele Bannister, David Fleming, Daniela Huppenkothen, Kevin Heng, Jason Curtis, Chloe Fisher, James Davenport, and Erik Tollerud. We are also indebted to Thomas Affatigato, who first showed the author Praesepe through a telescope in 2006, and who planted other important seeds that made this work possible. This work has been carried out in the framework of the PlanetS National Centre of Competence in Research (NCCR) supported by the Swiss National Science Foundation (SNSF). This paper includes data collected by the *Kepler* mission. Funding for the *Kepler* mission is provided by the NASA Science Mission directorate. This paper includes data collected by the *TESS* mission. Funding for the *TESS* mission is provided by the NASA Explorer Program. This research has made use of NASA's Astrophysics Data System. This research has made use of the VizieR catalog access tool, CDS, Strasbourg, France (<http://vizier.unistra.fr/>). The original description of the VizieR service was published in Ochsenbein et al. (2000). Some of the results in this paper have been derived using the healpy and HEALPix package.

⁴ <https://github.com/bmorris3/birthmarks>

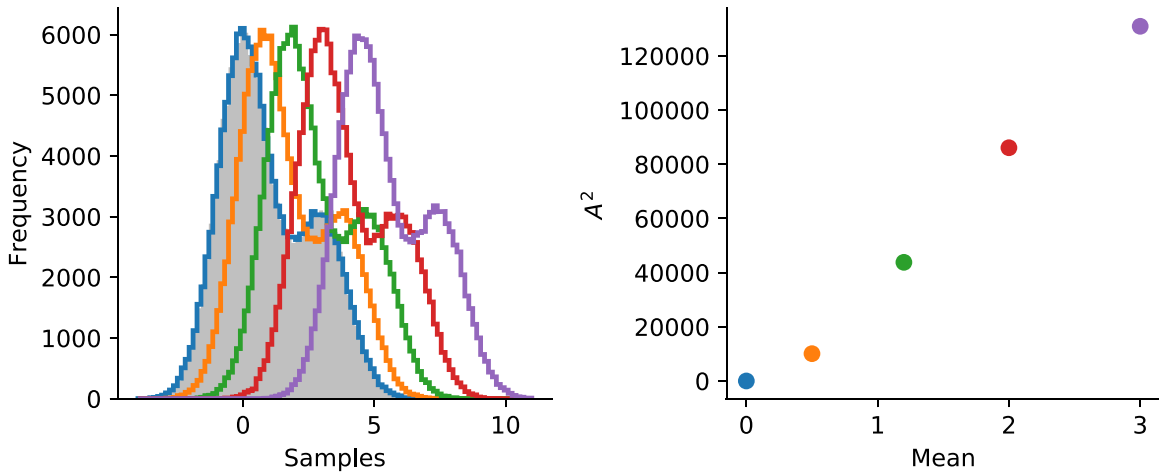


Figure 11. Demonstration of the behavior and dynamic range of the `scipy` implementation of the k -sample Anderson–Darling statistic A^2 when comparing pairs of bimodal distributions. The colored distributions on the left panel are compared with the gray-filled distribution, and the corresponding Anderson–Darling statistic is shown on the right panel with the same color. We chose a bimodal distribution for this example to illustrate that the Anderson–Darling statistic makes no assumption about the distributions being compared. The Anderson–Darling statistic for the sample with $\mu = 0$ is $A^2 \approx -0.6$.

Software: `astropy` (Astropy Collaboration et al. 2013, 2018), `ipython` (Perez & Granger 2007), `numpy` (Van Der Walt et al. 2011), `scipy` (Jones et al. 2001), `matplotlib` (Hunter 2007), `scikit-learn` (Pedregosa et al. 2011), `corner` (Foreman-Mackey 2016), `astroquery` (Ginsburg et al. 2019), `lightkurve` (Lightkurve Collaboration et al. 2018), `photutils` (Bradley et al. 2016), `healpy` (Górski et al. 2005; Zonca et al. 2019), `emcee` (Foreman-Mackey et al. 2013).

Facilities: *Kepler*, *TESS*.

Appendix Anderson–Darling Statistic

The k -sample Anderson–Darling statistic is a non-parametric test of the null hypothesis that two groups of data are drawn from identical distributions. We use the `scipy` implementation of the k -sample Anderson–Darling statistic, which varies from approximately -1.3 to $>10^5$, for distributions that are nearly identical and easily distinguishable, respectively. An exact description of the algorithm for computing the Anderson–Darling statistic can be found in Scholz & Stephens (1987). A demonstration of the behavior and dynamic range of the Anderson–Darling statistic when comparing pairs of samples is given in Figure 11.

ORCID iDs

Brett M. Morris  <https://orcid.org/0000-0003-2528-3409>

References

- Akeret, J., Refregier, A., Amara, A., Seehars, S., & Hasner, C. 2015, *JCAP*, **8**, 043
- Alsubai, K., Mislis, D., Tsvetanov, Z. I., et al. 2017, *AJ*, **153**, 200
- Anderson, T. W., & Darling, D. A. 1952, *Ann. Math. Stat.*, **23**, 193
- Astropy Collaboration, Price-Whelan, A. M., Sipőcz, B. M., et al. 2018, *AJ*, **156**, 123
- Astropy Collaboration, Robitaille, T. P., Tollerud, E. J., et al. 2013, *A&A*, **558**, A33
- Baliunas, S. L., Donahue, R. A., Soon, W. H., et al. 1995, *ApJ*, **438**, 269
- Barnes, S. A., Weingrill, J., Fritzewski, D., Strassmeier, K. G., & Platais, I. 2016, *ApJ*, **823**, 16
- Berdyugina, S. V. 2005, *LRSP*, **2**, 8
- Borucki, W. J., Koch, D., Basri, G., et al. 2010, *Sci*, **327**, 977
- Borucki, W. J., Koch, D. G., Basri, G., et al. 2011, *ApJ*, **736**, 19
- Bradley, L., Sipőcz, B., Robitaille, T., et al. 2016, *astropy/photutils*: v0.3, Zenodo, doi:10.5281/zenodo.164986
- Bruno, G., Lewis, N. K., Alam, M. K., et al. 2019, *MNRAS*, **491**, 5361
- Bruno, G., Lewis, N. K., Stevenson, K. B., et al. 2018, *AJ*, **156**, 124
- Christiansen, J. L., Jenkins, J. M., Caldwell, D. A., et al. 2012, *PASP*, **124**, 1279
- Ciardi, D. R., Crossfield, I. J. M., Feinstein, A. D., et al. 2018, *AJ*, **155**, 10
- Corsaro, E., Lee, Y.-N., García, R. A., et al. 2017, *NatAs*, **1**, 0064
- Curtis, J. L., Agüeros, M. A., Douglas, S. T., & Meibom, S. 2019a, *ApJ*, **879**, 49
- Curtis, J. L., Agüeros, M. A., Mamajek, E. E., Wright, J. T., & Cummings, J. D. 2019b, *AJ*, **158**, 77
- David, T. J., Cody, A. M., Hedges, C. L., et al. 2019a, *AJ*, **158**, 79
- David, T. J., Petigura, E. A., Luger, R., et al. 2019b, *ApJL*, **885**, L12
- Douglas, S. T., Agüeros, M. A., Covey, K. R., & Kraus, A. 2017, *ApJ*, **842**, 83
- Foreman-Mackey, D. 2016, *JOSS*, **1**, 24
- Foreman-Mackey, D., Hogg, D. W., Lang, D., & Goodman, J. 2013, *PASP*, **125**, 306
- Gagné, J., Mamajek, E. E., Malo, L., et al. 2018, *ApJ*, **856**, 23
- Gaia Collaboration, Brown, A. G. A., Vallenari, A., et al. 2018, arXiv:1804.09365
- Giles, H. A. C., Collier Cameron, A., & Haywood, R. D. 2017, *MNRAS*, **472**, 1618
- Ginsburg, A., Sipőcz, B. M., Brasseur, C. E., et al. 2019, *AJ*, **157**, 98
- Gonzalez, G. 2016a, *MNRAS*, **459**, 1060
- Gonzalez, G. 2016b, *MNRAS*, **463**, 3513
- Górski, K. M., Hivon, E., Banday, A. J., et al. 2005, *ApJ*, **622**, 759
- Gully-Santiago, M. A., Herczeg, G. J., Czekala, I., et al. 2017, *ApJ*, **836**, 200
- Hall, J. C. 2008, *LRSP*, **5**, 2
- Hébrard, G., Collier Cameron, A., Brown, D. J. A., et al. 2013, *A&A*, **549**, A134
- Howard, R., Gilman, P. I., & Gilman, P. A. 1984, *ApJ*, **283**, 373
- Howell, S. B., Sobek, C., Haas, M., et al. 2014, *PASP*, **126**, 398
- Hunter, J. D. 2007, *CSE*, **9**, 90
- Jackson, R. J., & Jeffries, R. D. 2013, *MNRAS*, **431**, 1883
- Järvinen, S. P., Strassmeier, K. G., Carroll, T. A., Ilyin, I., & Weber, M. 2018, *A&A*, **620**, A162
- Jones, E., Oliphant, T., Peterson, P., et al. 2001, *SciPy: Open Source Scientific Tools for Python*, <http://www.scipy.org/>
- Karoff, C., Metcalfe, T. S., Santos, A. R. G., et al. 2018, *ApJ*, **852**, 46
- Kenyon, S. J., & Hartmann, L. 1995, *ApJS*, **101**, 117
- Kirk, J., Wheatley, P. J., Louden, T., et al. 2016, *MNRAS*, **463**, 2922
- Kovacs, G. 2018, *A&A*, **612**, L2
- Lanza, A. F. 2016, in *Imaging Surface Spots from Space-Borne Photometry*, ed. J.-P. Rozelot & C. Neiner (Cham: Springer International), 43
- Lightkurve Collaboration, Cardoso, J. V. D. M. A., Hedges, C., et al. 2018, *Lightkurve: Kepler and TESS Time Series Analysis in Python*, Astrophysics Source Code Library, ascl:1812.013
- Lintusaari, J., Gutmann, M. U., Dutta, R., Kaski, S., & Corander, J. 2016, *Syst. Biol.*, **66**, e66

- Lomb, N. R. 1976, [Ap&SS](#), **39**, 447
- Mandel, K., & Agol, E. 2002, [ApJL](#), **580**, L171
- Mann, A. W., Gaidos, E., Vanderburg, A., et al. 2017, [AJ](#), **153**, 64
- Mann, A. W., Vanderburg, A., Rizzuto, A. C., et al. 2017, [AJ](#), **155**, 4
- McQuillan, A., Mazeh, T., & Aigrain, S. 2014, [ApJS](#), **211**, 24
- Meibom, S., Barnes, S. A., Latham, D. W., et al. 2011, [ApJL](#), **733**, L9
- Meingast, S., Alves, J., & Fürnkranz, V. 2019, [A&A](#), **622**, L13
- Morris, B. M., Agol, E., Davenport, J. R. A., & Hawley, S. L. 2018, [MNRAS](#), **476**, 5408
- Morris, B. M., Davenport, J. R. A., Giles, H. A. C., et al. 2019, [MNRAS](#), **484**, 3244
- Morris, B. M., Hebb, L., Davenport, J. R. A., Rohn, G., & Hawley, S. L. 2017, [ApJ](#), **846**, 99
- Newton, E. R., Mann, A. W., Tofflemire, B. M., et al. 2019, [ApJL](#), **880**, L17
- Ochsenbein, F., Bauer, P., & Marcout, J. 2000, [A&AS](#), **143**, 23
- Önehag, A., Korn, A., Gustafsson, B., Stempels, E., & Vandenberg, D. A. 2011, [A&A](#), **528**, A85
- Pecaut, M. J., & Mamajek, E. E. 2016, [MNRAS](#), **461**, 794
- Pedregosa, F., Varoquaux, G., Gramfort, A., et al. 2011, *J. Mach. Learn. Res.*, **12**, 2825
- Perez, F., & Granger, B. E. 2007, [CSE](#), **9**, 21
- Pettersen, B. R., Hawley, S. L., & Fisher, G. H. 1992, [SoPh](#), **142**, 197
- Press, W. H., & Rybicki, G. B. 1989, [ApJ](#), **338**, 277
- Ricker, G. R., Winn, J. N., Vanderspek, R., et al. 2014, [Proc. SPIE](#), **9143**, 914320
- Schmitt, J. R., Agol, E., Deck, K. M., et al. 2014, [ApJ](#), **795**, 167
- Scholz, F. W., & Stephens, M. A. 1987, *J. Am. Stat. Assoc.*, **82**, 918
- Schrijver, C. J., Cote, J., Zwaan, C., & Saar, S. H. 1989, [ApJ](#), **337**, 964
- Silva Aguirre, V., Davies, G. R., Basu, S., et al. 2015, [MNRAS](#), **452**, 2127
- Sisson, S. A., Fan, Y., & Beaumont, M. A. 2018, [arXiv:1802.09720](#)
- Skumanich, A. 1972, [ApJ](#), **171**, 565
- Solanki, S. K. 2003, [A&ARv](#), **11**, 153
- Sonett, C. P., Giampapa, M. S., & Matthews, M. S. 1991, *The Sun in Time* (Tucson, AZ: Univ. Arizona Press)
- Strassmeier, K. G., & Rice, J. B. 1998, [A&A](#), **330**, 685
- Sun, L., Ioannidis, P., Gu, S., et al. 2019, [A&A](#), **624**, A15
- Sunnåker, M., Busetto, A. G., Numminen, E., et al. 2013, [PLSCB](#), **9**, e1002803
- Van Der Walt, S., Colbert, S. C., & Varoquaux, G. 2011, [CSE](#), **13**, 22
- Zonca, A., Singer, L., Lenz, D., et al. 2019, [JOSS](#), **4**, 1298